Pure Silica with Ordered Silanols for Propylene/Propane Adsorptive Separation Unraveled by Three-Dimensional Electron Diffraction

Jing Wang, Chao Ma, Jiaqi Liu, Yi Liu, Xiaoqiu Xu, Miao Xie, Hao Wang, Lei Wang,* Peng Guo,* and Zhongmin Liu

Read Online

ACCESS | Metrics & More | Article Recommendations | Supporting Information

ABSTRACT: Adsorptive separation of propylene (C_3H_6) from propane (C_3H_8), which could deal with energy-intensive cryogenic distillation technologies, remains challenging due to their similar physiochemical properties. Herein, we present a pure silica zeolite with ordered silanols (OSs), whose crystallographic structure was unraveled by the advanced three-dimensional electron diffraction (3D ED), displaying the highly efficient separation of propylene from propane under ambient conditions. The 3D ED technique enables us to investigate its 8-ring pore opening transformation from the round one to the elliptical one during the removal of organic structure-directing agents. Such unique elliptical 8-ring pore openings can exclude larger-size propane and only adsorb propylene. Its C_3H_6/C_3H_8 separation performance is also confirmed by column breakthrough experiments, showing a high dynamic adsorption capacity of 53.36 cm^3 g^{-1} for C_3H_6 but negligible C_3H_8 under ambient conditions. The dynamic capacity for C_3H_6 is superior to that of the well-known pure silica **DDR**-type zeolite (31.07 cm^3 g^{-1}). The density functional theory calculation demonstrates that the adsorbed propylene is distributed in the heart-shaped cavity and has a weak interaction with the OSs.

3D Electron Diffraction
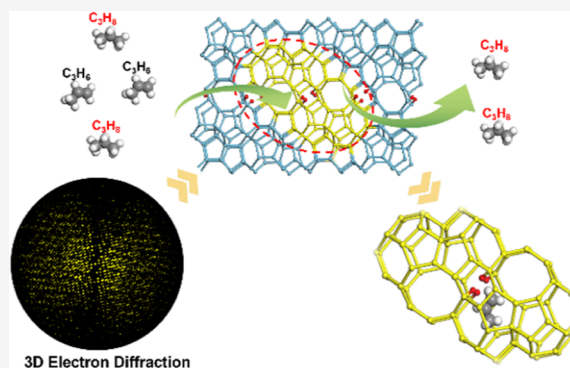
INTRODUCTION

Propylene, as an essential building block for various petrochemical manufacturers, is produced via steam cracking of naphtha or field nature gas,[1] fluid catalytic cracking of gas oils,[2] and other methods (i.e., MTO and PDH).[2,3] Its saturated counterpart propane is inevitably present as the associated gas which should be removed since propylene applications are closely guided by their purity grades. Polymer-grade specifications require a high purity with a 99.5 weight % (wt %) minimum, while the chemical-grade ones involve a propylene purity of 92% or higher. The physicochemical properties of propylene (C_3H_6) and propane (C_3H_8) differ only slightly, as evidenced by a small discrepancy in boiling points (approximately 5 K) and kinetic diameters (less than 0.4 Å). To separate C_3H_6 from C_3H_8, the cryogenic distillation technique has been conventionally utilized; however, it is quite costly and energy intensive due to the close boiling/condensation points between both components. From the energy conservation and environmental protection points of view, adsorptive separation based on high-efficiency and low-cost porous solids represents an alternative approach for separating C_3H_6/C_3H_8.

In recent years, various porous materials have been studied as suitable adsorbents, such as mesoporous carbon materials, clays, resins, zeolites, metal−organic frameworks (MOFs),[4−8] covalent organic frameworks (COFs),[9−12] and hydrogen-

bonded organic frameworks (HOFs).[13−17] Among them, emerging MOFs, COFs, and HOFs hold promise as adsorbents for hydrocarbon separations benefiting from their inherent advantages, including excellent tunability in their pore size, shape, and surface functionality.[4,11,17] Nevertheless, the relatively low thermal stability, expensive linker, and difficult regeneration may impede the practical application as a promising adsorbent.

Compared with these novel porous materials, conventional zeolites composed of TO_4 (T = Si, Al, P, etc.) as basic building units are crystalline porous materials with ordered channels or cavities, which still play crucial roles in industrial catalysis, gas separation, and gas storage. Among these significant industrial zeolites, pure silica zeolites have drawn increasing attention due to their hydrothermal stabilities,[18−20] promising separation applications,[21,22] and structural dynamics.[23,24] The silanol in the pure silica zeolite is a crucially important factor since it can affect its catalytic performance,[25−32] tune hydrophilicity and hydrophobicity,[33−35] and provide open sites for further
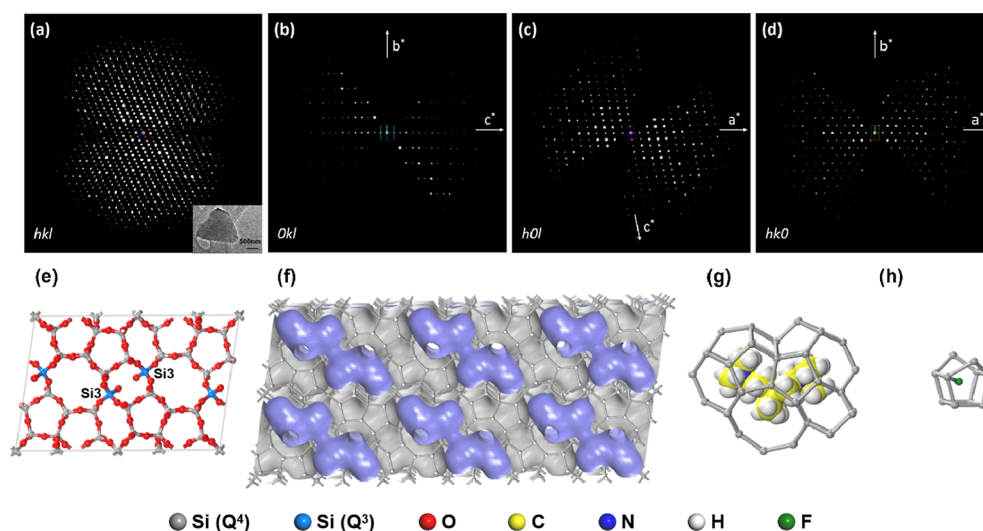
Figure 1. (a) 3D reciprocal lattice of ITQ-55-as reconstructed from the cRED data. Insert is the TEM image of the ITQ-55 nanocrystal from which the cRED data were collected. (b–d) 2D slices of 0kl, h0l, and hk0. The reflection conditions are hkl: $h + k = 2n$, 0kl: $k = 2n$, h0l: $h = 2n$, hk0: $h + k = 2n$, and h00: $h = 2n$. The possible space groups are C2, Cm, and C2/m. (e) 3D projections of the framework structure solved by cRED along the [010] direction, showing the terminal silanol groups and the less elliptical 8-ring pore openings. Bridging oxygen atoms in the framework have been omitted for clarity; (f) unique channel system of ITQ-55; (g,h) locations of OSDA in the heart-shaped cavity and fluoride ion in the bea cage determined through Rietveld refinement.

functionalization.[26,36−38] Therefore, probing the locations of silanols at the atomic level enables us to understand pore openings, channel connectives, and active sites arising from the presence of silanols, which will further affect the following structure−activity relationship, especially for small gas molecule separation and alkane/alkene separation.

Nowadays, there are a variety of conventional approaches to characterize silanols. For instance, Fourier transform infrared (FTIR) spectroscopy can provide a typical bond vibration at $3300-3750$ cm^{-1}, while solid-state magic angle spinning (MAS) nuclear magnetic resonance (NMR) could provide significant chemical shifts of coordination around $1.3-2.2$ ppm for ^{1}H and -90 to -105 ppm for ^{29}Si,[26,31,32] respectively. However, these methods are challenging to identify the atomic coordinates of silanols. When silanols are distributed orderly, diffraction methods (X-ray diffraction and electron diffraction) can be utilized as powerful tools to identify their locations at the atomic level. Although traditional single-crystal X-ray diffraction (SCXRD) can be competent for the structure solution (solving the initial structural model from the diffraction data) and the following structural refinement, this approach has a strict requirement on the crystal size (at least larger than 20 μm). Unfortunately, industrial zeolites normally crystalize in nano-sizes that are too small to be investigated by SCXRD. Conventional powder X-ray diffraction (PXRD) can explore the structural information of nanocrystals at the atomic level; however, the ambiguity in assigning diffraction intensities due to the peak overlapping, disorder, undesirable impurities in bulk materials, and so forth hinder further investigations.[39,40]

Recently, the emerging three-dimensional (3D) electron diffraction (ED) technique has been able to collect 3D structural information in a reciprocal space from one individual nanocrystal.[41−48] The unit cell parameters, space groups, and even the atomic coordinates can be obtained from the 3D ED data set. More recently, continuous rotation electron diffraction (cRED), one of the 3D ED techniques, not only solves crystallographic structures of nanocrystals but also further refines their structures against high-quality 3D ED data.

It is attributed to the fact that such a technique can collect 3D ED data in a short time (minimizing structural deterioration caused by electrons) and greatly enhance ED data quality through 3D intensity integration. Although this unique technique has explored a variety of fascinating functional materials[49,50] and biology macromolecules,[51,52] the pure silica zeolite with ordered silanols (OSs) revealed by cRED is quite rare.

In this work, we report a pure silica zeolite with OSs whose crystallographic structure is unraveled by cRED. It is closely related to a four-connected ITQ-55 zeolite. The cRED technique enables us to monitor the structural evolution from ITQ-55 with OSs to fully four-connected ITQ-55 at the atomic level. Compared with elliptical 8 ring in the four-connected ITQ-55, less elliptical 8-ring pore openings delimited by Q^3 Si(OH) (OSi)$_3$ and Q^4 Si(OSi)$_4$ are present in the ITQ-55 with OSs, which shows the promising C$_3$H$_6$/C$_3$H$_8$ separation performance.

RESULTS AND DISCUSSION

Identification of Structural Transformation during the Calcination. ITQ-55 was first reported by Corma's group in 2017, which was synthesized by a complex organic structural directing agent (OSDA) $N^2,N^2,N^2,N^5,N^5,N5,3a6a$-octamethyloctahydropentalene-2,5-diammonium cation. After the calcination of as-made ITQ-55 in the air at 800 °C (denoted as ITQ-55-air-800), it has shown promising separation performance in ethane/ethylene.[22] PXRD patterns of as-made ITQ-55 (designated ITQ-55-as) and ITQ-55-air-800 are distinct (Figure S1a), indicating that crystallographic structures of ITQ-55 materials change during the calcination process. Such an interesting phenomenon inspired us to further probe its structural transformation in detail.

Structure Determination of ITQ-55-as by cRED. A high-quality 3D ED data set from one individual nanocrystal of ITQ-55-as (resolution: 0.86 Å; completeness: 76.3%; 720 ED frames ranging from -48.5 to $67.8°$) was collected within 3 min, and the reconstructed 3D reciprocal space is illustrated in
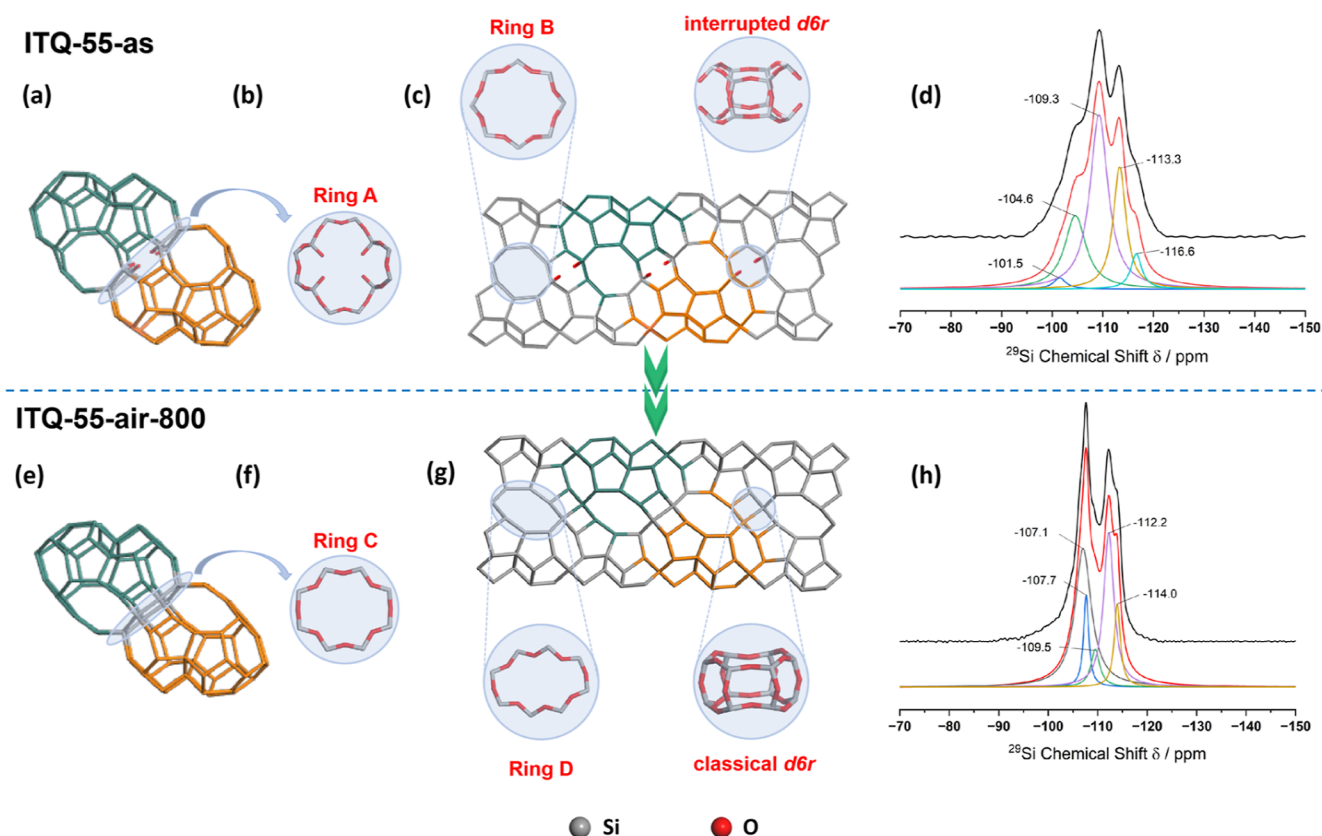
Figure 2. Structural comparisons of ITQ-55-as and ITQ-55-air-800. (a,e) Heart-shaped cages (highlighted in green and orange) in both structures; (b,f) inter-connection 8 rings; (c,g) projections along the [010] direction of ITQ-55-as and ITQ-air-800 structures; ring B and interrupted *d6r* in ITQ-55-as and ring D and classical *d6r* in ITQ-55-air-800 are enlarged for clarity. (d,h) ^{29}Si MAS NMR spectra of ITQ-55-as and ITQ-55-air-800.

Figure 1a. The monoclinic unit cell parameters could be deduced from this data set, and possible space groups (*C2*, *Cm*, and *C2/m*) can be obtained based on the reflection conditions as demonstrated in Figure 1b−d. Subsequently, the direct methods implemented in SHELXT were applied to this 3D data set for the initial structure solution. It turns out that all the 10 T and 23 O atoms in the asymmetric unit can be identified, and it is worth noting that Si3 connects with three Si atoms through bridging oxygen atoms, leaving one terminal silicon hydroxyl group (Figure 1e, Tables S1 and S2). It indicates that ITQ-55-as has OSs. ITQ-55-as can be considered as the assembly of heart-shaped zeolite cavities (Figures 1f and 2a). In the ac-plane at the same height, a pair of heart-shaped zeolite cavities are connected through 8 ring denoted as ring A (Figure 2b). Pairs of heart-shaped cavities in ITQ-55-as are linked with adjacent pairs through ring B along the *b*-axis, generating a 2D channel system (Figures 1f, 2c, and S1b−g). As illustrated in Figure S2, peaks in the solid-state ^{1}H−^{13}C cross-polar MAS NMR spectrum from ITQ-55-as were in good agreement with those in the liquid ^{13}C NMR spectrum from the pure OSDA, confirming that it was kept intact during the synthesis process. Locations of OSDAs and fluoride ions were determined through Rietveld refinement against PXRD data. It is of significance to note that there are three possible isomers of OSDAs which are challenging to determine based on the diffraction method (Figure S3). Therefore, we calculated the potential energies of different isomers within a heart-shaped cavity and found that isomer III was the most matched conformation with a relative energy of −3.99 eV (Figure S4). When isomer III was considered as a rigid-body fragment and

the simulated annealing algorithms implemented in TOPAS-V5.0 was further employed to determine its initial position, final Rietveld refinement results converged R_{wp} 3.37% and GOF 2.302 (as displayed in Figure S5a and Table S3). It shows that the complicated OSDA and fluoride ion are located in the heart-shaped cavity and *bea* cage (Figure 1g,h), respectively.

Structural Comparisons between ITQ-55-as and ITQ-55-air-800. It would be of interest to compare ITQ-55-as with ITQ-55-air-800. As shown in Figure 2e, a pair of heart-shaped cavities observed in ITQ-55-air-800 are connected through elliptical 8 rings (denoted as ring C, as displayed in Figure 2f). It is quite distinct from the scenario observed in ITQ-55-as that contains ring A decorated with four silanols as illustrated in Figure 2b. More importantly, the elliptical 8-ring pore openings (denoted as ring D shown in Figure 2g) of cavities are observed in the ITQ-55-air-800 structure, while less elliptical ring B could be identified in ITQ-55-as. The interesting and unique OSs result in the interrupted double 6 rings (*d6rs*) in ITQ-55-as (Figure 2c). After the calcination, OSs disappear while the classical *d6rs* emerge in ITQ-55-air-800 (Figure 2g). Such structural transformation was also supported by the ^{29}Si solid-state MAS NMR technique. The ^{29}Si signals at −104.6 and −101.5 ppm (Figure 2d) arising from Q^3 species[31] are present in ITQ-55-as, which are different from scenarios observed in ITQ-55-air-800 (Figure 2h). These striking structural features, OSs, are responsible for maintaining the pore opening of ring B as the main diffusion pathway.

Propylene/Propane Adsorptive Separation. To explore the separation performance of ITQ-55 with OSs, OSDAs occluded in its cavities should be removed, and simultaneously

OSs will be maintained. It is challenging to obtain pure phase ITQ-55 with OSs and without OSDAs in the cavities calcined in the air (Figure S6). It results from the fact that a lower calcined temperature results in the incomplete combustion of OSDA, while a higher one facilitates OSs to fuse, generating the four-connected ITQ-55-air-800 phase (Figure S6). Therefore, we attempt to calcine as-made samples in the presence of ozone at different temperatures, removing OSDAs at a lower temperature. A series of samples were calcined at temperatures ranging from 200 to 600 °C and denoted as ITQ-55-O3-T (T: calcination temperature) as illustrated in Figure S7. It turns out that ITQ-55-O3-400 maintains the structural features of OSs. The effective removal of OSDAs within their cavities has also been confirmed by FTIR spectroscopy (Figure S8).

Subsequently, the cRED technique was also utilized to characterize the crystallographic structure and directly validate the preservation of OSs in the ITQ-55-O3-400 sample (Figures 3a, S9, Tables S1, and S4). The ^{29}Si solid-state
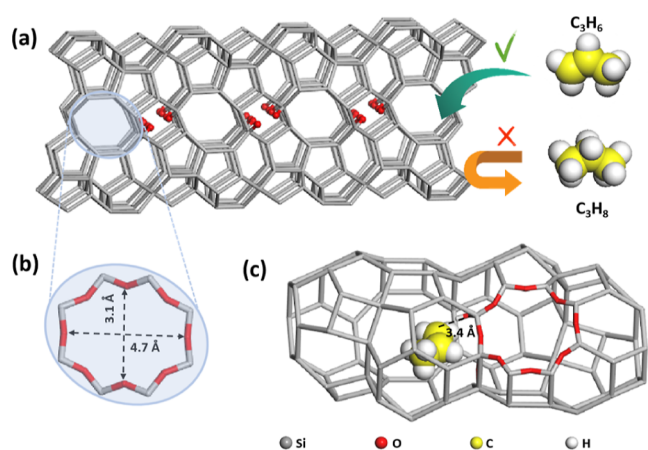
Figure 3. (a) Structural model of ITQ-55-O3-400 solved by cRED; (b) its elliptical 8-ring pore opening; (c) location of adsorbed propylene within the heart-shaped cavity and its interaction with the OS, which are investigated by density functional theory (DFT) calculations.

MAS NMR spectrum of ITQ-55-O3-400 exhibited peaks at −104.9 and −101.6 ppm (Figure S10), which is similar to ITQ-55-as and further supports the preservation of OSs in the ITQ-55-O3-400 sample. The vibrational features of SiOH

within ITQ-O3-400 were also probed by FTIR spectroscopy as displayed in Figure S11.

Moreover, the crystallographic structure of ITQ-55-O3-400 is also confirmed by Rietveld refinement against high-quality PXRD data (Figure S5b and Table S3). It is of interest to note that its 8-ring pore opening is approximately 4.7 Å × 3.1 Å as shown in Figure 3b. The Ar adsorption isotherm at 87 K is conducted (Figure S12), revealing the microporous nature of ITQ-55-O3-400 with the saturated adsorption of 229 cm^3 g^{-1} at 1 bar. The Brunauer−Emmett−Teller surface area is calculated as 648 m^2 g^{-1}. Furthermore, ITQ-55-O3-400 demonstrated excellent thermal stability of up to approximately 400 °C and remarkable resistance to chemical treatments, as verified by the PXRD analysis illustrated in Figure S13. All such features indicate that ITQ-55-O3-400 might be a promising adsorbent for olefin/paraffin separation.

The single-component adsorption isotherms of C$_3$H$_6$ and C$_3$H$_8$ were collected at 298 K. A notable amount of C$_3$H$_6$ (59.25 cm^3 g^{-1}) was adsorbed by ITQ-55-O3-400 at 298 K and 1 bar, while there was a negligible amount of C$_3$H$_8$ adsorption (2.31 cm^3 g^{-1}) under the identical condition as shown in Figure 4a. The C$_3$H$_6$ uptakes were found to be consistently maintained across five successive adsorption−desorption cycles (as evidenced in Figure S14a,b), indicating its excellent stability and recycling capacity. In addition, kinetic adsorption measurements at 298 K and 1 bar were conducted as demonstrated in Figure S14c,d. It indicated that the uptake of C$_3$H$_6$ and C$_3$H$_8$ was comparable to those in Figure 4a and that the adsorption rate of C$_3$H$_6$ was much faster than that of C$_3$H$_8$. Based on adsorption isotherms at 273 and 298 K, the isosteric heat of adsorption (Q_{st}) at zero loading was calculated as 29.3 kJ mol^{-1} using the virial method (Figure S15a−c). The heat of adsorption is quite low compared with those of MOFs,[53−55] indicating that ITQ-55-O3-400 is desirable for facile regeneration under mild conditions. Moreover, the ideal adsorbed solution theory[56] selectivity was calculated as >10^3 between 0 and 1 bar at 298 K (Figure S15d).

Motivated by the selective molecular exclusion of ITQ-55-O3-400 shown by the single component adsorption, we further evaluated its C$_3$H$_6$/C$_3$H$_8$ separation performance by carrying out binary gas (C$_3$H$_6$/C$_3$H$_8$, 50/50, v/v) column breakthrough measurements. Since **DDR**-type pure silica zeolite has been considered as the promising adsorbent for separating C$_3$H$_6$/C$_3$H$_8$, it is selected as the reference adsorbent. C$_3$H$_8$ was eluted at the very beginning of the process, indicating no noticeable adsorption of C$_3$H$_8$ in the column, whereas C$_3$H$_6$ underwent a
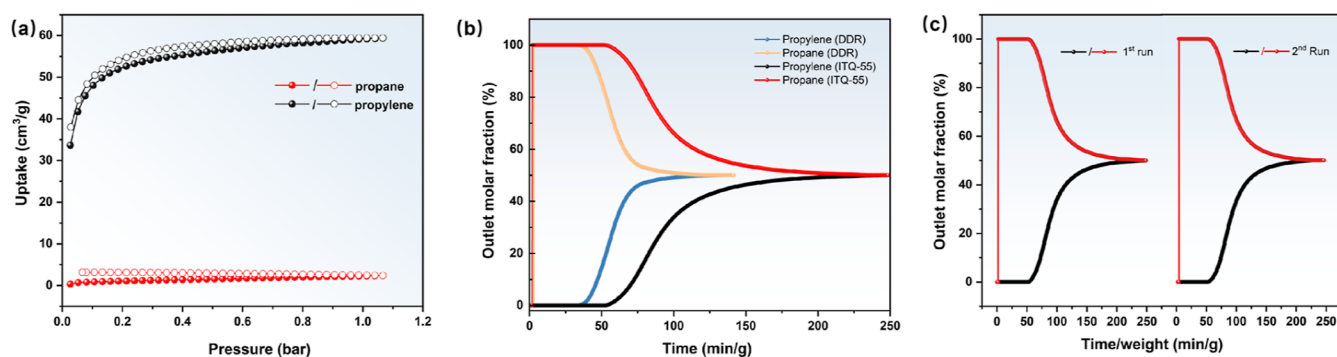
Figure 4. (a) Adsorption isotherms of propylene and propane on ITQ-55-O3-400 at 298 K. (b) Comparison of column breakthrough performance between the **DDR**-type pure silica zeolite and ITQ-55-O3-400 adsorbents. (c) Two consecutive column breakthrough runs with an equimolar propane/propylene binary mixture feed at room temperature. Red symbols, propane; black symbols, propylene.

long retention time of ~51.04 and 39.19 min g^{-1} (Figure 4b) for ITQ-55-O3-400 and **DDR**-type pure silica zeolite, respectively. Correspondingly, the dynamic propylene adsorption capacity of ITQ-55-O3-400 was calculated as 53.36 cm^3 g^{-1}, which is higher than that of the **DDR**-type pure silica zeolite (31.07 cm^3 g^{-1}). Repeated runs of column breakthrough measurements in the separation of C$_3$H$_6$/C$_3$H$_8$ revealed essentially no loss of adsorption capacity, suggesting the excellent recyclability of ITQ-55-O3-400 (Figure 4c). More importantly, DFT calculations demonstrate that the adsorbed propylene molecule is distributed in the heart-shaped cavity, interacting with the OS through the weak hydrogen bonding (Si—OH···C $_{propylene}$) (Figure 3c).

CONCLUSIONS

In summary, pure silica zeolite with OSs was directly unraveled by the 3D ED technique at the atomic level. The OSs can not only maintain the proper elliptical 8-ring pore opening size but also offer a weak interaction site with the adsorbed propylene molecules, achieving the promising C$_3$H$_6$/C$_3$H$_8$ separation performance. The deeper understanding of the structural features of ITQ-55 with OSs is expected to enable further development toward new superior adsorbents for advanced adsorptive separation technologies.

EXPERIMENTAL SECTION

Preparation of ITQ-55-as. The OSDAs were directly purchased from Wuhan Sun-shine Bio-technology Co., Ltd. Before usage, iodine-form OSDAs were exchanged into the hydroxyl form with Ag$_2$O (Aladdin reagents, 99%). Then, the concentration of the OSDA aqueous solution was determined by titration with a standard HCl solution (1 M). Typically, 1.25 g silica gel (Ludox-AS40, 40% wt.) was added into the 8.36 g OSDA solution (7.18% wt.) with vigorous stirring. Once the clear solution formed, 0.21 g HF (40% wt.) was added dropwise. Afterward, the white paste was dried in an oven at 353 K overnight to remove excess water. Finally, the gel with the general composition—SiO$_2$/0.25 OSDA(OH)$_2$/0.5 HF/5 H$_2$O—was transferred into a 25 mL Teflon-lined autoclave and reacted at 433 K for 14 days. The as-made zeolite white powders were obtained by filtration, washed with deionized water, and dried in an air oven at 373 K overnight.

Preparations of ITQ-55-O3-400 and ITQ-55-air-800. ITQ-55-O3-400 was obtained by calcination of ITQ-55-as at 673 K for 12 h in the presence of ozone. The as-made powders were placed in a quartz tube, and 130 g/Nm^3 ozone was then introduced into the tube at a constant flow rate of 0.6 cm^3 min^{-1}. The ozone was produced by an electrical discharge ozone generator (OSAN-CFG), and the ozone concentration entering the unit was monitored by an ozone gas analyzer (UVOS-3300) purchased from OSAN Environmental and Technology (Dalian) Co., Ltd. ITQ-55-air-800 was prepared by the calcination of ITQ-55-as at 1073 K for 6 h in air.

Powder X-ray Diffraction. The PXRD data for the phase identification were collected on a Bruker D8 ADVANCE equipped with the Cu Kα radiation source (λ = 1.5418 Å) at 40 kV and 40 mA. The whole pattern was collected in the 2θ range of 5−50° with the increment of 0.2°/s at a fixed step size of 0.015°. The temperature-dependent PXRD was recorded on an Empyrean X-ray Diffractometer equipped with an in situ heating cell of XRK900 from Anton-Paar. The measurement parameters included a scan speed of 4.5°/min and a scan range of 2θ from 5 to 40°. The high-resolution PXRD data for Rietveld refinement were collected on the STOE STADP diffractometer with a monochromatic Cu Kα1 source (λ = 1.5406 Å) in the Debye−Scherrer geometry. The PXRD data were collected in the 0.2 mm capillary. The whole Rietveld refinement was performed with TOPAS academic suite V5.0. The Rietveld refinement process is described as follows: the Pawley fitting was performed against the high-resolution PXRD data of the as-made zeolite ITQ-55,

and it turns out that unit cell parameters are a = 23.4640 Å, b = 13.23943 Å, c = 15.4005 Å, and β = 97.7305°. The structural model solved by cRED was further optimized based on the experimental unit cell parameters. It means that the geometry restraints of Si—O: 1.61 Å, O—T—O: 109.5°, and T—O—T: 145° with proper weights were imposed on the target zeolite framework. After optimizing the zeolite framework, the scale factor was calculated by using the 2theta angle region of 45−105° and then applied to the whole pattern. In this case, the difference electron density map was obtained, which corresponds to OSDAs occluded in the cage and missing fluoride ions. Based on the DFT calculations (see below), it turns out that isomer III matches the framework well. Therefore, the initial location of isomer III was obtained by the simulated annealing algorithm implemented in TOPAS academic suite V5.0. Final Rietveld refinement results are displayed in Table S3.

Electron Microscopy. The selected area electron diffraction (SAED) patterns for reconstructing 3D ED cRED data were collected on JEOL 2100plus equipped with an ASI camera at 200 kV. The obtained series of SAED patterns were reconstructed by REDp software. Scanning electron microscopy was performed on a Hitachi SU8020 microscope with an accelerating voltage of 2 kV.

FTIR and Physical Sorption. FTIR spectra of ITQ-55-as, ITQ-55-O3-400, and ITQ-55-air-800 in the region of 400−4000 cm^{-1} (resolution: 4 cm^{-1}) were measured using KBr containing pellets on a Bruker Tensor 27 spectrophotometer at room temperature as shown in Figure S8. In order to remove the effect from water, ITQ-55-O3-400 and ITQ-55-air-800 were pretreated at 300 °C for 60 min in vacuum. FTIR spectra of ITQ-55-O3-400 and ITQ-55-air-800 in the region of 2500−4000 cm^{-1} (Figure S11) were collected on a Bruker Tensor 27 instrument equipped with an MCT detector. Self-supported wafers of both samples (20 mg) were placed into an in situ quartz cell equipped with CaF$_2$ windows. Physical adsorption of Ar was performed on a Micromeritics ASAP 2460 Version 3.00 analyzer at 87 K. Physical adsorption of N$_2$ was performed on a Micromeritics 3Flex analyzer at 77 K. Before the adsorption, the calcined zeolite was activated for 4 h at 623 K. The specific surface area and pore size distribution were evaluated by the adsorption branch. The time-dependent kinetic adsorption isotherms were collected at 100 kPa on a BSD-DVS instrument from Beishide Instrument Technology (Beijing) Co., Ltd.

NMR. Liquid state ^{13}C NMR was collected on a Bruker AVANCE 400 spectrometer at a resonance frequency of 100.6 MHz. Solid-state ^{29}Si MAS NMR experiments were performed on a Bruker AVANCE III 600 spectrometer at a resonance frequency of 119.2 MHz. ^{29}Si MAS NMR spectra with high-power proton decoupling were recorded on a 4 mm probe with a spinning rate of 10 kHz, a π/4 pulse length of 2.6 μs, and a recycle delay of 80 s. The chemical shifts of ^{29}Si were referenced to TMS.

Determination of OSDA Configuration by DFT Calculation. In this work, the single-point energy calculations were performed at the level of B3LYP[57] with the 6-31G(d) basis set for all atoms. All DFT calculations were performed using the Gaussian 16 program.[58] A pure silica fragment containing the heart-shaped cavity and the *bea* CBU was cut from the 3D framework, and it was terminated by the OH group. The positive charges from OSDAs were balanced by the two fluoride ions which were determined by PXRD refinement. Single-point energies between the framework and OSDAs with three configurations (Figure S4) were calculated by DFT calculations. The final results show that isomer III is more favorable for the framework.

Determination of Adsorbed Propylene (C$_3$H$_6$) Molecules in a Pair of Heart-Shaped Cavities by DFT Calculations. A pair of heart-shaped cavities' structural model was generated using Material Studio[59] program. To simplify the calculation, the case of one C$_3$H$_6$ molecule adsorbed within a pair of heart-shaped cavities was taken. Ten different C$_3$H$_6$ adsorption sites were predicted by employing the adsorption locator module involving the Monte Carlo method in statistical mechanics combined with the COMPASS II force field. They were further optimized by DFT in CP2K package.[60] To ensure the sufficient convergence, the auxiliary plane wave grid cutoff was set as 500 Ry. They were geometrically optimized using Perdew−Burke−

Ernzerhof gradient-corrected exchange correlation functional,[61] and Grimme's semi-empirical DFT-D3 scheme of dispersion correction was adopted to describe the van der Waals interactions within the cavities.[62] The most stable one is displayed in Figure 3c.

Breakthrough Measurements. Breakthrough tests were carried out in an auto mixed-gas breakthrough apparatus (3P MIXSORB) using a stainless-steel column (I.D. 6 mm, length 100 mm). The adsorbents were activated at 350 °C under helium purging (10 mL/min). When the temperature cooled down to 25 °C, helium flow was stopped and the feed mixed gases (C_3H_6/C_3H_8, 50/50, v/v) at a flow rate of 1 mL/min were introduced into the adsorption column. The outlet gas was analyzed by using a mass spectrometer (MKS). The adsorbent was heated at 473 K under helium flow for 1 h for regeneration.

ASSOCIATED CONTENT

Ⓢ Supporting Information

The Supporting Information is available free of charge at https://pubs.acs.org/doi/10.1021/jacs.2c13847.

> Notes and synthetic procedures for material preparation, PXRD, 3D ED, solid-state ^{29}Si MAS NMR, physical sorption profiles and atomic coordinates, and other addition information (PDF)

Accession Codes

CCDC 2210945 and 2210953 contain the supplementary crystallographic data for this paper. These data can be obtained free of charge via www.ccdc.cam.ac.uk/data_request/cif, or by emailing data_request@ccdc.cam.ac.uk, or by contacting The Cambridge Crystallographic Data Centre, 12 Union Road, Cambridge CB2 1EZ, UK; fax: +44 1223 336033.

AUTHOR INFORMATION

Corresponding Authors

Lei Wang − *School of Chemistry and Molecular Engineering, Nanjing Tech University, Nanjing 211816, China;* ⓞ orcid.org/0000-0002-4520-0685; Email: l_wang19@njtech.edu.cn

Peng Guo − *National Engineering Research Center of Lower-Carbon Catalysis Technology, Dalian National Laboratory for Clean Energy, Dalian Institute of Chemical Physics, Chinese Academy of Sciences, Dalian 116023 Liaoning, China; University of Chinese Academy of Sciences, Beijing 100049, China;* ⓞ orcid.org/0000-0001-5392-3915; Email: pguo@dicp.ac.cn

Authors

Jing Wang − *National Engineering Research Center of Lower-Carbon Catalysis Technology, Dalian National Laboratory for Clean Energy, Dalian Institute of Chemical Physics, Chinese Academy of Sciences, Dalian 116023 Liaoning, China;* ⓞ orcid.org/0000-0002-4185-0373

Chao Ma − *National Engineering Research Center of Lower-Carbon Catalysis Technology, Dalian National Laboratory for Clean Energy, Dalian Institute of Chemical Physics, Chinese Academy of Sciences, Dalian 116023 Liaoning, China; University of Chinese Academy of Sciences, Beijing 100049, China*

Jiaqi Liu − *Hoffmann Institute of Advanced Materials, Shenzhen Polytechnic, Shenzhen 518055, China*

Yi Liu − *State Key Laboratory of Fine Chemicals, School of Chemical Engineering, Dalian University of Technology, Dalian 116024, China*

Xiaoqiu Xu − *College of Science, Institute for Frontier and Interdisciplinary Sciences, Zhejiang University of Technology, Hangzhou 310014 Zhejiang, China*

Miao Xie − *Institute of Functional Nano & Soft Materials (FUNSOM), Jiangsu Key Laboratory for Carbon-Based Functional Materials & Devices, Soochow University, Suzhou 215123, China;* ⓞ orcid.org/0000-0002-9797-1449

Hao Wang − *Hoffmann Institute of Advanced Materials, Shenzhen Polytechnic, Shenzhen 518055, China;* ⓞ orcid.org/0000-0001-7732-778X

Zhongmin Liu − *National Engineering Research Center of Lower-Carbon Catalysis Technology, Dalian National Laboratory for Clean Energy, Dalian Institute of Chemical Physics, Chinese Academy of Sciences, Dalian 116023 Liaoning, China; University of Chinese Academy of Sciences, Beijing 100049, China*

Complete contact information is available at:
https://pubs.acs.org/10.1021/jacs.2c13847

Author Contributions

The manuscript was written through contributions of all authors. All authors have given approval to the final version of the manuscript.

Notes

The authors declare no competing financial interest.

ACKNOWLEDGMENTS

REFERENCES

(1) Fakhroleslam, M.; Sadrameli, S. M. Thermal Cracking of Hydrocarbons for the Production of Light Olefins; A Review on Optimal Process Design, Operation, and Control. *Ind. Eng. Chem. Res.* **2020**, *59*, 12288−12303.

(2) Monai, M.; Gambino, M.; Wannakao, S.; Weckhuysen, B. M. Propane to olefins tandem catalysis: a selective route towards light olefins production. *Chem. Soc. Rev.* **2021**, *50*, 11503−11529.

(3) Nawaz, Z. Light alkane dehydrogenation to light olefin technologies: a comprehensive review. *Rev. Chem. Eng.* **2015**, *31*, 413−436.

(4) Furukawa, H.; Cordova, K. E.; O'Keeffe, M.; Yaghi, O. M. The Chemistry and Applications of Metal-Organic Frameworks. *Science* **2013**, *341*, 1230444.

(5) Peng, Y.; Li, Y.; Ban, Y.; Jin, H.; Jiao, W.; Liu, X.; Yang, W. Metal-organic framework nanosheets as building blocks for molecular sieving membranes. *Science* **2014**, *346*, 1356−1359.

(6) Li, L.; Lin, R.-B.; Krishna, R.; Li, H.; Xiang, S.; Wu, H.; Li, J.; Zhou, W.; Chen, B. Ethane/ethylene separation in a metal-organic framework with iron-peroxo sites. *Science* **2018**, *362*, 443−446.

(7) Chen, K.-J.; Madden, D. G.; Mukherjee, S.; Pham, T.; Forrest, K. A.; Kumar, A.; Space, B.; Kong, J.; Zhang, Q.-Y.; Zaworotko, M. J. Synergistic sorbent separation for one-step ethylene purification from a four-component mixture. *Science* **2019**, *366*, 241−246.

(8) Cai, G.; Yan, P.; Zhang, L.; Zhou, H.-C.; Jiang, H.-L. Metal-Organic Framework-Based Hierarchically Porous Materials: Synthesis and Applications. *Chem. Rev.* **2021**, *121*, 12278−12326.

(9) Dawson, R.; Cooper, A. I.; Adams, D. J. Nanoporous organic polymer networks. *Prog. Polym. Sci.* **2012**, *37*, 530−563.

(10) Colson, J. W.; Dichtel, W. R. Rationally synthesized two-dimensional polymers. *Nat. Chem.* **2013**, *5*, 453−465.

(11) Trickett, C. A.; Helal, A.; Al-Maythalony, B. A.; Yamani, Z. H.; Cordova, K. E.; Yaghi, O. M. The chemistry of metal-organic frameworks for CO_2 capture, regeneration and conversion. *Nat. Rev. Mater.* **2017**, *2*, 17045.

(12) Lohse, M. S.; Bein, T. Covalent Organic Frameworks: Structures, Synthesis, and Applications. *Adv. Funct. Mater.* **2018**, *28*, 1705553.

(13) Luo, X.-Z.; Jia, X.-J.; Deng, J.-H.; Zhong, J.-L.; Liu, H.-J.; Wang, K.-J.; Zhong, D.-C. A Microporous Hydrogen-Bonded Organic Framework: Exceptional Stability and Highly Selective Adsorption of Gas and Liquid. *J. Am. Chem. Soc.* **2013**, *135*, 11684−11687.

(14) Wang, H.; Li, B.; Wu, H.; Hu, T.-L.; Yao, Z.; Zhou, W.; Xiang, S.; Chen, B. A Flexible Microporous Hydrogen-Bonded Organic Framework for Gas Sorption and Separation. *J. Am. Chem. Soc.* **2015**, *137*, 9963−9970.

(15) Li, P.; He, Y.; Zhao, Y.; Weng, L.; Wang, H.; Krishna, R.; Wu, H.; Zhou, W.; O'Keeffe, M.; Han, Y.; Chen, B. A Rod-Packing Microporous Hydrogen-Bonded Organic Framework for Highly Selective Separation of C_2H_2/CO_2 at Room Temperature. *Angew. Chem., Int. Ed.* **2015**, *54*, 574−577.

(16) Karmakar, A.; Illathvalappil, R.; Anothumakkool, B.; Sen, A.; Samanta, P.; Desai, A. V.; Kurungot, S.; Ghosh, S. K. Hydrogen-Bonded Organic Frameworks (HOFs): A New Class of Porous Crystalline Proton-Conducting Materials. *Angew. Chem., Int. Ed.* **2016**, *55*, 10667−10671.

(17) Lin, R.-B.; He, Y.; Li, P.; Wang, H.; Zhou, W.; Chen, B. Multifunctional porous hydrogen-bonded organic framework materials. *Chem. Soc. Rev.* **2019**, *48*, 1362−1389.

(18) Corma, A.; Rey, F.; Rius, J.; Sabater, M. J.; Valencia, S. Supramolecular self-assembled molecules as organic directing agent for synthesis of zeolites. *Nature* **2004**, *431*, 287−290.

(19) Weston, S. C.; Peterson, B. K.; Gatt, J. E.; Lonergan, W. W.; Vroman, H. B.; Afeworki, M.; Kennedy, G. J.; Dorset, D. L.; Shannon, M. D.; Strohmaier, K. G. EMM-17, a New Three-Dimensional Zeolite with Unique 11-Ring Channels and Superior Catalytic Isomerization Performance. *J. Am. Chem. Soc.* **2019**, *141*, 15910−15920.

(20) Liu, X.; Liu, L.; Pan, T.; Yan, N.; Dong, X.; Li, Y.; Chen, L.; Tian, P.; Han, Y.; Guo, P.; Liu, Z. The Complex Crystal Structure and Abundant Local Defects of Zeolite EMM-17 Unraveled by Combined Electron Crystallography and Microscopy. *Angew. Chem., Int. Ed.* **2021**, *60*, 24227−24233.

(21) Jee, S. E.; Sholl, D. S. Carbon Dioxide and Methane Transport in DDR Zeolite: Insights from Molecular Simulations into Carbon Dioxide Separations in Small Pore Zeolites. *J. Am. Chem. Soc.* **2009**, *131*, 7896−7904.

(22) Bereciartua, P. J.; Cantín, Á.; Corma, A.; Jordá, J. L.; Palomino, M.; Rey, F.; Valencia, S.; Corcoran, E. W.; Kortunov, P.; Ravikovitch, P. I.; Burton, A.; Yoon, C.; Wang, Y.; Paur, C.; Guzman, J.; Bishop, A. R.; Casty, G. L. Control of zeolite framework flexibility and pore topology for separation of ethane and ethylene. *Science* **2017**, *358*, 1068−1071.

(23) Jordá, J. L.; Rey, F.; Sastre, G.; Valencia, S.; Palomino, M.; Corma, A.; Segura, A.; Errandonea, D.; Lacomba, R.; Manjón, F. J.; Gomis, Ó.; Kleppe, A. K.; Jephcoat, A. P.; Amboage, M.; Rodríguez-Velamazán, J. A. Synthesis of a Novel Zeolite through a Pressure-Induced Reconstructive Phase Transition Process. *Angew. Chem., Int. Ed.* **2013**, *52*, 10458−10462.

(24) Santamaría-Pérez, D.; Marqueño, T.; MacLeod, S.; Ruiz-Fuertes, J.; Daisenberger, D.; Chuliá-Jordan, R.; Errandonea, D.; Jordá, J. L.; Rey, F.; McGuire, C.; Mahkluf, A.; Kavner, A.; Popescu, C. Structural Evolution of CO2-Filled Pure Silica LTA Zeolite under High-Pressure High-Temperature Conditions. *Chem. Mater.* **2017**, *29*, 4502−4510.

(25) Dubray, F.; Dib, E.; Medeiros-Costa, I.; Aquino, C.; Minoux, D.; van Daele, S.; Nesterenko, N.; Gilson, J.-P.; Mintova, S. The challenge of silanol species characterization in zeolites. *Inorg. Chem. Front.* **2022**, *9*, 1125−1133.

(26) Medeiros-Costa, I. C.; Dib, E.; Nesterenko, N.; Dath, J. P.; Gilson, J.-P.; Mintova, S. Silanol defect engineering and healing in zeolites: opportunities to fine-tune their properties and performances. *Chem. Soc. Rev.* **2021**, *50*, 11156−11179.

(27) Zhou, H.; Yi, X.; Hui, Y.; Wang, L.; Chen, W.; Qin, Y.; Wang, M.; Ma, J.; Chu, X.; Wang, Y.; Hong, X.; Chen, Z.; Meng, X.; Wang, H.; Zhu, Q.; Song, L.; Zheng, A.; Xiao, F.-S. Isolated boron in zeolite for oxidative dehydrogenation of propane. *Science* **2021**, *372*, 76−80.

(28) Fernández, A. B.; Boronat, M.; Blasco, T.; Corma, A. Establishing a Molecular Mechanism for the Beckmann Rearrangement of Oximes over Microporous Molecular Sieves. *Angew. Chem., Int. Ed.* **2005**, *44*, 2370−2373.

(29) Chu, Y.; Ji, P.; Yi, X.; Li, S.; Wu, P.; Zheng, A.; Deng, F. Strong or weak acid, which is more efficient for Beckmann rearrangement reaction over solid acid catalysts? *Catal. Sci. Technol.* **2015**, *5*, 3675−3681.

(30) Marthala, V. R. R.; Jiang, Y.; Huang, J.; Wang, W.; Gläser, R.; Hunger, M. Beckmann Rearrangement of 15N-Cyclohexanone Oxime on Zeolites Silicalite-1, H-ZSM-5, and H-[B]ZSM-5 Studied by Solid-State NMR Spectroscopy. *J. Am. Chem. Soc.* **2006**, *128*, 14812−14813.

(31) Baerlocher, C.; Xie, D.; McCusker, L. B.; Hwang, S.-J.; Chan, I. Y.; Ong, K.; Burton, A. W.; Zones, S. I. Ordered silicon vacancies in the framework structure of the zeolite catalyst SSZ-74. *Nat. Mater.* **2008**, *7*, 631−635.

(32) Prodinger, S.; Derewinski, M. A.; Vjunov, A.; Burton, S. D.; Arslan, I.; Lercher, J. A. Improving Stability of Zeolites in Aqueous Phase via Selective Removal of Structural Defects. *J. Am. Chem. Soc.* **2016**, *138*, 4408−4415.

(33) Li, S.; Li, Z.; Medina, D.; Lew, C.; Yan. Organic-Functionalized Pure-Silica-Zeolite MFI Low-k Films. *Chem. Mater.* **2005**, *17*, 1851−1854.

(34) Eslava, S.; Urrutia, J.; Busawon, A. N.; Baklanov, M. R.; Iacopi, F.; Aldea, S.; Maex, K.; Martens, J. A.; Kirschhock, C. E. A. Zeolite-Inspired Low-kDielectrics Overcoming Limitations of Zeolite Films. *J. Am. Chem. Soc.* **2008**, *130*, 17528−17536.

(35) Wang, C.; Guo, H.; Leng, S.; Yu, J.; Feng, K.; Cao, L.; Huang, J. Regulation of hydrophilicity/hydrophobicity of aluminosilicate zeolites: a review. *Crit. Rev. Solid State Mater. Sci.* **2021**, *46*, 330−348.

(36) Smeets, S.; Berkson, Z. J.; Xie, D.; Zones, S. I.; Wan, W.; Zou, X.; Hsieh, M.-F.; Chmelka, B. F.; McCusker, L. B.; Baerlocher, C. Well-Defined Silanols in the Structure of the Calcined High-Silica Zeolite SSZ-70: New Understanding of a Successful Catalytic Material. *J. Am. Chem. Soc.* **2017**, *139*, 16803−16812.

(37) Grosso-Giordano, N. A.; Hoffman, A. S.; Boubnov, A.; Small, D. W.; Bare, S. R.; Zones, S. I.; Katz, A. Dynamic Reorganization and Confinement of TiIV Active Sites Controls Olefin Epoxidation Catalysis on Two-Dimensional Zeotypes. *J. Am. Chem. Soc.* **2019**, *141*, 7090−7106.

(38) Schroeder, C.; Mück-Lichtenfeld, C.; Xu, L.; Grosso-Giordano, N. A.; Okrut, A.; Chen, C.-Y.; Zones, S. I.; Katz, A.; Hansen, M. R.; Koller, H. A Stable Silanol Triad in the Zeolite Catalyst SSZ-70. *Angew. Chem., Int. Ed.* **2020**, *59*, 10939−10943.

(39) Baerlocher, C.; Gramm, F.; Massüger, L.; McCusker, L. B.; He, Z.; Hovmöller, S.; Zou, X. Structure of the Polycrystalline Zeolite Catalyst IM-5 Solved by Enhanced Charge Flipping. *Science* **2007**, *315*, 1113−1116.

(40) Guo, P.; Shin, J.; Greenaway, A. G.; Min, J. G.; Su, J.; Choi, H. J.; Liu, L.; Cox, P. A.; Hong, S. B.; Wright, P. A.; Zou, X. A zeolite family with expanding structural complexity and embedded isoreticular structures. *Nature* **2015**, *524*, 74−78.

(41) Kolb, U.; Gorelik, T.; Kübel, C.; Otten, M. T.; Hubert, D. Towards automated diffraction tomography: Part I-Data acquisition. *Ultramicroscopy* **2007**, *107*, 507−513.

(42) Kolb, U.; Gorelik, T.; Otten, M. T. Towards automated diffraction tomography. Part II-Cell parameter determination. *Ultramicroscopy* **2008**, *108*, 763−772.

(43) Kolb, U.; Krysiak, Y.; Plana-Ruiz, S. Automated electron diffraction tomography - development and applications. *Acta Crystallogr., Sect. B: Struct. Sci., Cryst. Eng. Mater.* **2019**, *75*, 463−474.

(44) Wan, W.; Sun, J.; Su, J.; Hovmöller, S.; Zou, X. Three-dimensional rotation electron diffraction: software RED for automated data collection and data processing. *J. Appl. Crystallogr.* **2013**, *46*, 1863−1873.

(45) Smeets, S.; Zou, X.; Wan, W. Serial electron crystallography for structure determination and phase analysis of nanocrystalline materials. *J. Appl. Crystallogr.* **2018**, *51*, 1262−1273.

(46) Nannenga, B. L.; Shi, D.; Leslie, A. G. W.; Gonen, T. High-resolution structure determination by continuous-rotation data collection in MicroED. *Nat. Methods* **2014**, *11*, 927−930.

(47) Shi, D.; Nannenga, B. L.; Iadanza, M. G.; Gonen, T. Three-dimensional electron crystallography of protein microcrystals. *eLife* **2013**, *2*, No. e01345.

(48) Palatinus, L.; Corrêa, C. A.; Steciuk, G.; Jacob, D.; Roussel, P.; Boullay, P.; Klementová, M.; Gemmi, M.; Kopeček, J.; Domeneghetti, M. C.; Cámara, F.; Petříček, V. Structure refinement using precession electron diffraction tomography and dynamical diffraction: tests on experimental data. *Acta Crystallogr., Sect. B: Struct. Sci., Cryst. Eng. Mater.* **2015**, *71*, 740−751.

(49) Ding, H.; Li, J.; Xie, G.; Lin, G.; Chen, R.; Peng, Z.; Yang, C.; Wang, B.; Sun, J.; Wang, C. An AIEgen-based 3D covalent organic framework for white light-emitting diodes. *Nat. Commun.* **2018**, *9*, 5234.

(50) Lenzen, D.; Zhao, J.; Ernst, S.-J.; Wahiduzzaman, M.; Ken Inge, A.; Fröhlich, D.; Xu, H.; Bart, H.-J.; Janiak, C.; Henninger, S.; Maurin, G.; Zou, X.; Stock, N. A metal-organic framework for efficient water-based ultra-low-temperature-driven cooling. *Nat. Commun.* **2019**, *10*, 3025.

(51) Xu, H.; Lebrette, H.; Yang, T.; Srinivas, V.; Hovmöller, S.; Högbom, M.; Zou, X. A Rare Lysozyme Crystal Form Solved Using Highly Redundant Multiple Electron Diffraction Datasets from Micron-Sized Crystals. *Structure* **2018**, *26*, 667−675.

(52) Xu, H.; Lebrette, H.; Clabbers, M. T. B.; Zhao, J.; Griese, J. J.; Zou, X.; Högbom, M. Solving a new R2lox protein structure by microcrystal electron diffraction. *Sci. Adv.* **2019**, *5*, No. eaax4621.

(53) Cadiau, A.; Adil, K.; Bhatt, P. M.; Belmabkhout, Y.; Eddaoudi, M. A metal-organic framework-based splitter for separating propylene from propane. *Science* **2016**, *353*, 137−140.

(54) Liang, B.; Zhang, X.; Xie, Y.; Lin, R.-B.; Krishna, R.; Cui, H.; Li, Z.; Shi, Y.; Wu, H.; Zhou, W.; Chen, B. An Ultramicroporous Metal-Organic Framework for High Sieving Separation of Propylene from Propane. *J. Am. Chem. Soc.* **2020**, *142*, 17795−17801.

(55) Wang, H.; Dong, X.; Colombo, V.; Wang, Q.; Liu, Y.; Liu, W.; Wang, X.-L.; Huang, X.-Y.; Proserpio, D. M.; Sironi, A.; Han, Y.; Li, J. Tailor-Made Microporous Metal-Organic Frameworks for the Full Separation of Propane from Propylene Through Selective Size Exclusion. *Adv. Mater.* **2018**, *30*, 1805088.

(56) Myers, A. L.; Prausnitz, J. M. Thermodynamics of mixed-gas adsorption. *AIChE J.* **1965**, *11*, 121−127.

(57) Becke, A. D. Density-functional thermochemistry. III. The role of exact exchange. *J. Chem. Phys.* **1993**, *98*, 5648−5652.

(58) Frisch, M. J.; Trucks, G. W.; Schlegel, H. B.; Scuseria, G. E.; Robb, M. A.; Cheeseman, J. R.; Scalmani, G.; Barone, V.; Petersson, G. A.; Nakatsuji, H.; Li, X.; Caricato, M.; Marenich, A. V.; Bloino, J. B.; Janesko, G.; Gomperts, R.; Mennucci, B.; Hratchian, H. P.; OrtizIzmaylov, J. V. A. F.; Sonnenberg, J. L.; Williams-Young, D.; DingLipparini, F. F.; Egidi, F.; Goings, J.; Peng, B.; Petrone, A.; HendersonRanasinghe, T. D.; Zakrzewski, V. G.; Gao, J.; Rega, N.; Zheng, G.; Liang, W.; Hada, M.; Ehara, M.; Toyota, K.; Fukuda, R.; HasegawaIshida, J. M.; Nakajima, T.; Honda, Y.; Kitao, O.; Nakai, H.; VrevenThrossell, T. K.; Montgomery, J. A., Jr.; Peralta, J. E.; Ogliaro, F.; Bearpark, M. J.; Heyd, J. J.; Brothers, E. N.; Kudin, K. N.; Staroverov, V. N.; Keith, T. A.; Kobayashi, R.; Normand, J.; Raghavachari, K.; Rendell, A. P.; Burant, J. C.; Iyengar, S. S.; Tomasi, J.; Cossi, M.; Millam, J. M.; Klene, M.; Adamo, C.; Cammi, R.; Ochterski, J. W.; Martin, R. L.; Morokuma, K.; Farkas, O.; Foresman, J. B.; Fox, D. J. *Gaussian 16*. Revision A.03; Gaussian, Inc.: Wallingford CT, 2016.

(59) *Materials Studio*; Accelrys: San Diego.

(60) Kühne, T. D.; Iannuzzi, M. .; Del Ben, M.; Rybkin, V. V.; Seewald, P.; Stein, F.; Laino, T.; Khaliullin, R. Z.; Schütt, O.; Schiffmann, F.; Golze, D.; Wilhelm, J.; Chulkov, S.; Bani-Hashemian, M. H.; Weber, V.; Borštnik, U.; Taillefumier, M.; Jakobovits, A. S.; Lazzaro, A.; Pabst, H.; Müller, T.; Schade, R.; Guidon, M.; Andermatt, S.; Holmberg, N.; Schenter, G. K.; Hehn, A.; Bussy, A.; Belleflamme, F.; Tabacchi, G.; Glöß, A.; Bethune, I.; Mundy, C. J.; Plessl, C.; Watkins, M.; VandeVondele, J.; Krack, M.; Hutter, J. CP2K: An electronic structure and molecular dynamics software package - Quickstep: Efficient and accurate electronic structure calculations. *J. Chem. Phys.* **2020**, *152*, 194103.

(61) Perdew, J. P.; Burke, K.; Ernzerhof, M. Generalized Gradient Approximation Made Simple. *Phys. Rev. Lett.* **1996**, *77*, 3865−3868.

(62) Grimme, S.; Antony, J.; Ehrlich, S.; Krieg, H. A consistent and accurate ab initio parametrization of density functional dispersion correction (DFT-D) for the 94 elements H-Pu. *J. Chem. Phys.* **2010**, *132*, 154104.

🔖 Recommended by ACS